Naval Research Laboratory

Washington, DC 20375-5320

NRL/MR/6390--15-9621

Temperature Histories of Ti-6Al-4V Pulsed-Mode Laser Welds Calculated Using Multiple Constraints

S.G. LAMBRAKOS

Center for Computational Materials Science
Materials Science and Technology Division

A. SHABAEV

George Mason University
Fairfax, Virginia

August 12, 2015

REPORT DOCUMENTATION PAGE

Form Approved
OMB No. 0704-0188

1. REPORT DATE *(DD-MM-YYYY)*	**2. REPORT TYPE**	**3. DATES COVERED** *(From - To)*
12-08-2015	NRL Memorandum Report	

4. TITLE AND SUBTITLE

Temperature Histories of Ti-6Al-4V Pulsed-Mode Laser Welds Calculated Using Multiple Constraints

5a. CONTRACT NUMBER

5b. GRANT NUMBER

5c. PROGRAM ELEMENT NUMBER

6. AUTHOR(S)

S.G. Lambrakos and A. Shabaev[1]

5d. PROJECT NUMBER

5e. TASK NUMBER

5f. WORK UNIT NUMBER
63-4995-05

7. PERFORMING ORGANIZATION NAME(S) AND ADDRESS(ES)

Naval Research Laboratory, Code 6390
4555 Overlook Avenue, SW
Washington, DC 20375-5320

8. PERFORMING ORGANIZATION REPORT NUMBER

NRL/MR/6390--15-9621

9. SPONSORING / MONITORING AGENCY NAME(S) AND ADDRESS(ES)

Office of Naval Research
One Liberty Center
875 North Randolph Street, Suite 1425
Arlington, VA 22203-1995

10. SPONSOR / MONITOR'S ACRONYM(S)
ONR

11. SPONSOR / MONITOR'S REPORT NUMBER(S)

12. DISTRIBUTION / AVAILABILITY STATEMENT

Approved for public release; distribution is unlimited.

13. SUPPLEMENTARY NOTES

[1]George Mason University, Department of Computation and Data Sciences, Fairfax, VA 22030

14. ABSTRACT

Case study inverse thermal analyses of Ti-6Al-4V pulsed-mode laser welds are presented. These analyses employ a methodology that is in terms of numerical-analytical basis functions for inverse thermal analysis of steady state energy deposition in plate structures. The results of the case studies provide parametric representations of weld temperature histories that can be adopted as input data to various types of computational procedures, such as those for prediction of solid-state phase transformations. In addition, these temperature histories can be used to construct parametric-function representations for inverse thermal analysis of welds corresponding to other process parameters or welding processes whose process conditions are within similar regimes. The present study applies an inverse thermal analysis procedure that provides for the inclusion of volumetric constraint conditions whose two-dimensional projections are mappings onto transverse cross sections of experimentally measured solidification and transformation boundaries.

15. SUBJECT TERMS
Modeling of titanium welding

16. SECURITY CLASSIFICATION OF:			**17. LIMITATION OF ABSTRACT**	**18. NUMBER OF PAGES**	**19a. NAME OF RESPONSIBLE PERSON**
					Samuel G. Lambrakos
a. REPORT	**b. ABSTRACT**	**c. THIS PAGE**	Unclassified Unlimited	37	**19b. TELEPHONE NUMBER** *(include area code)*
Unclassified Unlimited	Unclassified Unlimited	Unclassified Unlimited			(202) 767-2601

Standard Form 298 (Rev. 8-98)
Prescribed by ANSI Std. Z39.18

Contents

Introduction

Case study inverse thermal analyses of Ti-6Al-4V pulsed-mode laser welds are presented. These analyses provide a parameterization of temperature histories for prediction of properties within the Heat Affected Zone (HAZ) of welds for the regime considered. The present study applies an inverse thermal analysis procedure that provides for the inclusion of volumetric constraint conditions whose two-dimensional projections are mappings onto transverse cross sections of experimentally measured solidification and transformation boundaries [1-3]. For the present study, which considers Ti-6Al-4V pulsed-mode laser welds, the phase transformation boundary adopted for temperature-field constraint conditions is that of the α to β phase transformation. The results of the case study analyses provide parametric representations of weld temperature histories that can be adopted as input data to various types of computational procedures, such as those for prediction of solid-state phase transformations and associated software implementations. In addition, these weld temperature histories can be adopted for inverse analysis of welds corresponding to other process parameters or welding processes whose process conditions are within similar regimes. The construction of temperature fields according to spatially and temporally distributed constraint conditions using linear combinations of basis functions represents a convenient approach to inverse analysis of energy deposition processes.

The formal structure underlying the inverse analysis approach applied in this study is that of parametric model representation of the temperature field in terms of numerical-analytical basis functions, and provides a general reduction of model complexity for purposes of weld analysis [1-3]. Reduction of model complexity is achieved by adopting analytical models for either the heat source or temperature field (or both) in combination with numerical methods.. A specific aspect of the inverse analysis methodology employed here, providing convenient adjustment of parameters, is construction of discrete volumetric source distributions. As discussed previously [1-3], the inverse modeling approach compensates for lack of information concerning material properties. The inverse method applied in this study is for the purpose of calculating temperature histories, and has various advantages for this specific purpose, which have been discussed previously [1-3]. The results of this study contribute to a continually evolving database of weld cross sections and temperature histories corresponding to specified weld processes, process conditions and types of metals and their alloys.

The organization of the subject areas presented are as follows. First, a brief description of the general procedure for inverse analysis of heat deposition processes is presented. Second, results of inverse thermal analyses of Ti-6Al-4V pulsed-mode laser welds are presented. These results provide a quantitative parametric representation of temperature histories for these welds and for any welds associated with similar welding process conditions. Third, a brief discussion is presented concerning specific aspects of the analysis results. Finally, a conclusion is given.

Inverse Analysis Procedure

Following the inverse analysis approach [4-7], a parametric model provides a means for the inclusion of information concerning the physical characteristics of a given energy deposition process [8]. Given the general trend features of temperature fields associated with welding processes, a consistent parametric representation of the temperature field for heat deposition within structures characterized by a finite thickness, in terms of numerical-analytical basis functions, is

Manuscript approved May 15, 2015.

$$T(\hat{x},t) = T_A + \sum_{k=1}^{N_k}\sum_{n=1}^{N_t} C(\hat{x}_k) G(\hat{x},\hat{x}_k,\kappa,n\Delta t,V) \tag{1a}$$

and

$$T(\hat{x}_n^c,t_n^c) = T_n^c\,, \tag{1b}$$

where

$$G(\hat{x},\hat{x}_k,t,\kappa,V) = \frac{1}{t}\exp\left[-\frac{(x-x_k-Vt)^2+(y-y_k)^2}{4\kappa t}\right] \times\left\{1+2\sum_{m=1}^{\infty}\exp\left[-\frac{\kappa m^2\pi^2 t}{l^2}\right]\cos\left[\frac{m\pi z}{l}\right]\cos\left[\frac{m\pi z_k}{l}\right]\right\}, \tag{2}$$

and

$$C(\hat{x}) = \sum_{k=1}^{N_k} Q(\hat{x}_k)\delta(\hat{x}-\hat{x}_k)\,. \tag{3}$$

where $Q(\hat{x}_k)$ is the value of the discrete source function at location $\hat{x}_k$. The quantities κ, V and l are the thermal diffusivity, welding speed and plate thickness, respectively. The procedure for inverse analysis defined by Eqs.(1)-(3) entails adjustment of the parameters $C(\hat{x}_k)$, $\hat{x}_k$ and Δt defined over the entire spatial region of the workpiece. Formally, this procedure entails adjustment of the steady state temperature field defined over the entire spatial region of the sample volume. This approach defines an optimization procedure where the temperature field spanning the spatial region of the sample volume is adopted as the quantity to be optimized. The constraint conditions are imposed on the temperature field spanning the bounded spatial domain of the workpiece by minimization of the value of the objective functions defined by

$$Z_T = \sum_{n=1}^{N} w_n\left(T(\hat{x}_n^c,t_n^c) - T_n^c\right)^2 \tag{4}$$

where T_n^c is the target temperature for position $\hat{x}_n^c = (x_n^c,y_n^c,z_n^c)$. The quantities w_n ($n=1,\ldots,N$) are weight coefficients that specify relative levels of influence associated with constraint conditions T_n^c.

The inverse analysis methodology defined by Eqs.(1)-(4) is based on a parametric numerical-analytical model, which combines numerical integration with optimization of linear combinations of numerical-analytical basis functions. In particular, Eq.(1a) defines a discrete numerical integration over time, where the time step Δt is specified according to the average energy deposited during the time Δt, for transition of the temperature field to steady state. It should be noted that the formulation of the inverse analysis methodology defined by Eq.(1)-(4) is equipped with a mathematical structure that satisfies all boundary conditions associated with welding of plate structures.

In addition to the parameters defined with respect to Eqs.(1)-(4), the parameteric model applied for inverse analysis includes a length scale parameter l_S, where in general $l_S < l$ defined by Eq.(2), for specification of the spatial scale of the calculated temperature field with respect to which parameters are adjusted. This length scale parameter provides for inclusion of more details of shape features of measured solidification boundaries to be adopted as constraint conditions. Accordingly, in the analyses that follow, two length parameters are considered, i.e., the plate thickness l and the depth l_S of the speciifed region of the temperature field to be calculated.

Table 1 Temperature field constraint conditions at positions (y_c,z_c) at solidification and transformation boundaries on transverse cross sections of Ti-6Al-4V welds

Solidification Boundaries

WELD 1	**WELD 2**	**WELD 3**	**WELD 4**	**WELD 5**
(y_c mm, z_c mm)	*(y_c mm, z_c mm)*	*(y_c mm, z_c mm)*	*(y_c mm, z_c mm)*	*(y_c mm, z_c mm)*
(1.252, 0.02846)	(1.592, 0.0370)	(1.439, 0.0369)	(2.384, 0.0769)	(1.615, 0.0769)
(1.195, 0.1423)	(1.481, 0.222)	(1.144, 0.2214)	(1.615, 0.3845)	(1.307, 0.3845)
(0.9676, 0.2846)	(1.222, 0.407)	(0.9594, 0.406)	(1.154, 0.769)	(0.923, 0.769)
(0.7115, 0.4269)	(1.037, 0.592)	(0.775, 0.590)	(1.000, 1.154)	(0.846, 1.154)
(0.4838, 0.5692)	(0.815, 0.7776)	(0.701, 0.775)	(0.731, 1.923)	(0.731, 1.538)
(0.313, 0.7115)	(0.5925, 0.963)	(0.664, 0.9594)	(.0769, 2.115)	(0.615, 1.923)
(0.02846, 0.7400)	(0.444, 1.1479)	(0.4797, 1.144)		(0.5383, 2.307)
	(0.0370, 1.2775)	(0.0369, 1.3284)		(0.0769, 2.538)
WELD 6	**WELD 7**	**WELD 8**	**WELD 9**	**WELD 10**
(y_c mm, z_c mm)	*(y_c mm, z_c mm)*	*(y_c mm, z_c mm)*	*(y_c mm, z_c mm)*	*(y_c mm, z_c mm)*
(1.622, 0.0811)	(1.738, 0.079)	(2.025, 0.075)	(3.525, 0.075)	(3.45, 0.075)
(1.379, 0.4055)	(1.501, 0.395)	(1.8, 0.375)	(3.45, 0.375)	(3.375, 0.375)
(1.2165, 0.8110)	(1.067, 0.790)	(1.088, 0.750)	(3.225, 0.75)	(3.30, 0.75)
(0.9732, 1.2165)	(0.869, 1.185)	(0.938, 1.125)	(2.925, 1.125)	(3.15, 1.125)
(0.8921, 1.622)	(0.751, 1.580)	(0.938, 1.50)	(2.55, 1.50)	(3.00, 1.50)
(0.6488, 2.028)	(0.751, 1.975)	(0.9, 1.875)	(2.025, 1.875)	(2.925, 1.875)
(0.608, 2.433)	(0.751, 2.370)	(0.6, 2.25)	(1.35, 2.25)	(2.775, 2.25)
(0.527, 2.8385)	(0.593, 2.765)	(0.075, 2.4)	(0.15, 2.55)	(2.70, 2.4)
	(0.237. 3.002)			(2.4, 3.0)

Transformation Boundaries

WELD 1	**WELD 2**	**WELD 3**	**WELD 4**	**WELD 5**
(y_c mm, z_c mm)	*(y_c mm, z_c mm)*	*(y_c mm, z_c mm)*	*(y_c mm, z_c mm)*	*(y_c mm, z_c mm)*
(1.5368, 0.02846)	(2.111, 0.0370)	(2.0664, 0.0369)	(3.461, 0.0769)	(2.6146, 0.0769)
(1.508, 0.1423)	(2.0737, 0.222)	(1.993, 0.2214)	(3.384, 0.3845)	(2.384, 0.3845)
(1.3945, 0.2846)	(1.9256, 0.4073)	(1.919, 0.406)	(3.153, 0.769)	(2.076, 0.769)
(1.1953, 0.4269)	(1.777, 0.5925)	(1.771, 0.590)	(2.845, 1.154)	(1.8456, 1.154)
(0.9676, 0.5692)	(1.555, 0.7776)	(1.5867, 0.775)	(2.307, 1.923)	(1.615, 1.538)
(0.6546, 0.7115)	(1.259, 0.9628)	(1.365 0.9594)	(1.692, 2.115)	(1.384, 1.923)
(0.2277, 0.8538)	(0.8887, 1.1479)	(1.070, 1.144)	(0.846, 2.307)	(1.00, 2.307)
	(0.6665, 1.296)	(0.701, 1.3284)	(.0769, 2.422)	(0.4614, 2.6915)
				(0.0769,2.7684)
WELD 6	**WELD 7**	**WELD 8**	**WELD 9**	**WELD 10**
(y_c mm, z_c mm)	*(y_c mm, z_c mm)*	*(y_c mm, z_c mm)*	*(y_c mm, z_c mm)*	*(y_c mm, z_c mm)*
(2.757, 0.0811)	(2.923, 0.079)	(3.225, 0.075)	(3.525, 0.075)	(3.45, 0.075)
(2.595, 0.4055)	(2.607, 0.395)	(3.15, 0.375)	(3.45, 0.375)	(3.375, 0.375)
(2.352, 0.8110)	(2.449, 0.790)	(3.075, 0.750)	(3.225, 0.75)	(3.30, 0.75)
(2.190, 1.2165)	(2.291, 1.185)	(2.85, 1.125)	(2.925, 1.125)	(3.15, 1.125)
(2.028, 1.622)	(1.975, 1.580)	(2.7, 1.50)	(2.55, 1.50)	(3.00, 1.50)
(1.784, 2.028)	(1.817, 1.975)	(2.4, 1.875)	(2.025, 1.875)	(2.925, 1.875)
(1.703, 2.433)	(1.659, 2.370)	(2.025, 2.25)	(1.35, 2.25)	(2.775, 2.25)
(1.622, 2.8385)	(1.659, 2.765)	(1.875, 2.4)	(0.15, 2.55)	(2.70, 2.4)
	(1.738. 3.002)	(1.725, 3.0)		(2.4, 3.0)

Inverse Thermal Analysis of Ti-6Al-4V Pulsed-Mode Laser Welds

In this section results of inverse thermal analyses of Ti-6Al-4V pulsed-mode laser welds are described, whose input power and pulse rate are adopted as process-control parameters. The significance of the inverse-problem approach for this type of analysis is that the nature of the coupling of the energy source to the workpiece, which is a function of beam power and process control parameters, is in principle difficult to specify relative to analysis based on the direct-problem approach. The Ti-6Al-4V welds, whose inverse analysis is presented here, consist of pulsed-mode laser welds described in reference [9].

The analysis presented here entails calculation of the steady state temperature field for a specified range of sizes and shapes of inner surface boundaries defined by the solidification boundary and by the transformation boundary associated with the α to β phase transformation of Ti-6Al-4V for a range of welding process parameters. The shapes of these boundaries are determined experimentally by analysis of transverse weld cross sections showing microstructure revealing solidification and transformation boundaries [9]. For calculations adopting the solidification boundaries as constraints, the parameter values assumed are $\kappa = 8.6 \times 10^{-6}$ m^2s^{-1}, T_M = 1604.85 ^oC. For calculations adopting the transformation boundaries as constraints, the parameter values assumed are $\kappa = 8.6 \times 10^{-6}$ m^2s^{-1}, T_{TB} = 995 ^oC. As discussed previously [1-3], reasonable estimates of κ and T_M are sufficient for inverse analysis. For this study, the same thermal diffusivity is assumed for calculation of temperature fields using solidification and transformation boundary constraints. This assumption is sufficient, within reasonable estimates, in that the set of parameters $C(\hat{x}_k)$, $k=1,...,N_k$, and κ are not uniquely determined by inverse analysis. Thus, changing estimated values of κ would require different values of $C(\hat{x}_k)$ in order to satisfy specified constraint conditions associated with T_M and T_{TB},. With respect to inverse analysis, the interpretation of κ as both an estimated material property and adjustable parameter is emphasized within the following.

The goal of the present analysis is determination of a set of parameters that can serve as initial estimates for parameter adjustment with respect to deep penetration welds of Ti and its alloys, whose process parameters are within similar regimes. Parameter adjustment with respect to other welds, which assume the results of this study as initial estimates, would adopt κ, T_M and T_{TB} as adjustable parameters, as well as the discrete source function $C(\hat{x}_k)$. Values of the workpiece thickness l and welding speed V defined in Eq. (2), and of the depth l_S of the region of interest, are given in the figures below. The upstream boundary constraints on the temperature field, $T_c = T_M$ and $T_c = T_{TB}$ for (y_c,z_c) defined in Eq. (1b), are given in Table 1 for the solidification and transformation boundaries. Given in Tables 2 through 21 are values of the discrete source function that have been calculated according to the constraint conditions and weld designations given in Table 1. The relative location of each discrete source is specified according to Fig.1. Shown in Figs. 2 through 36 are experimentally measured transverse weld cross sections of solidification and transformation boundaries [9], where weld process parmeters are given for each weld, and different planar slices of the steady state temperature field that have been calculated according to the constraint conditions given in Tables 1. Referring to the planer slices of the calculated temperature fields shown in these figures, it can be seen that all boundary conditions are satisfied, namely the condition $T(\hat{x},t) = T_M$ or $T(\hat{x},t) = T_{TB}$ at the solidification or

transformation boundary, respectively, and $\nabla T \cdot \hat{n} = 0$ at surface boundaries, where $\hat{n}$ is normal to the surface.

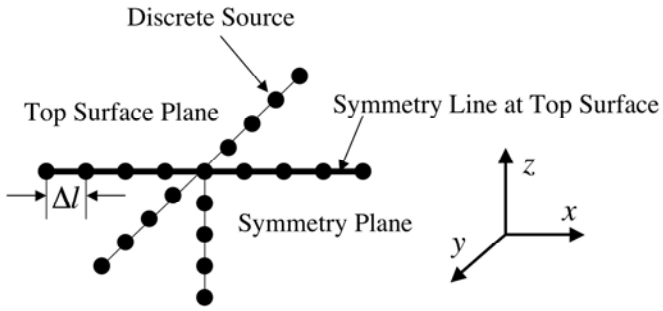

Fig. 1 Indexing scheme for relative locations of discrete sources $C(\hat{x}_k)$, $k=1,...,N_k$.

Table 2 Volumetric source function $C(\hat{x}_k)$ calculated according to solidification-boundary constraint conditions given in Table 1, where Δl = (0.996/60) mm (WELD 1).

k	C_k	(x_k y_k z_k) (Δl)
1	0.000	(0, 0, 1)
2	0.000	(0, 0, 5)
3	0.000	(0, 0, 10)
4	0.000	(0, 0, 15)
5	0.042	(0, 0, 20)
6	0.000	(0, 0, 25)
7	0.021	(0, 0, 30)
8	0.000	(0, 0, 35)
9	0.042	(0, 0, 40)
10	0.000	(0, 0, 45)
11	0.063	(0, 0, 50)
12	0.000	(0, 0, 55)
13	0.126	(0, 0, 60)
14	0.11	(-25, 0, 0)
15	0.11	(25, 0, 0)
16	0.11	(0,-25, 0)
17	0.11	(0, 25, 0)

Table 3 Volumetric source function $C(\hat{x}_k)$ calculated according to transformation-boundary constraint conditions given in Table 1, where Δl = (0.996/60) mm (WELD 1).

k	C_k	(x_k y_k z_k) (Δl)
1	0.000	(0, 0, 1)
2	0.000	(0, 0, 5)
3	0.000	(0, 0, 10)
4	0.000	(0, 0, 15)
5	0.016	(0, 0, 20)
6	0.000	(0, 0, 25)
7	0.008	(0, 0, 30)
8	0.000	(0, 0, 35)
9	0.016	(0, 0, 40)
10	0.000	(0, 0, 45)
11	0.024	(0, 0, 50)
12	0.000	(0, 0, 55)
13	0.096	(0, 0, 60)
14	0.090	(-25, 0, 0)
15	0. 090	(25, 0, 1)
16	0. 090	(0,-25, 1)
17	0. 090	(0, 25, 1)

Table 4 Volumetric source function $C(\hat{x}_k)$ calculated according to solidification-boundary constraint conditions given in Table 1, where Δl = (1.518/60) mm, $x_k = y_k = 0.0$ for k = 1 to 14 and $z_k = 1$ for k = 15 to 18 (WELD 2).

k	C_k	(x_k y_k z_k) (Δl)
1	0.000	(0, 0, 1)
2	0.000	(0, 0, 5)
3	0.000	(0, 0, 10)
4	0.000	(0, 0, 15)
5	0.252	(0, 0, 20)
6	0.000	(0, 0, 25)
7	0.108	(0, 0, 30)
8	0.000	(0, 0, 35)
9	0.072	(0, 0, 40)
10	0.000	(0, 0, 45)
11	0.024	(0, 0, 50)
12	0.108	(0, 0, 55)
13	0.144	(0, 0, 60)
14	0.288	(0, 0, 65)
15	0. 170	(-25, 0, 1)
16	0. 170	(25, 0, 1)
17	0. 170	(0,-25, 1)
18	0. 170	(0, 25, 1)

Table 5 Volumetric source function $C(\hat{x}_k)$ calculated according to transformation-boundary constraint conditions given in Table 1, where Δl = (1.518/60) mm, $x_k = y_k = 0.0$ for k = 1 to 13 and $z_k = 1$ for k = 14 to 17 (WELD 2).

k	C_k	(x_k y_k z_k) (Δl)
1	0.000	(0, 0, 1)
2	0.000	(0, 0, 5)
3	0.000	(0, 0, 10)
4	0.000	(0, 0, 15)
5	0.175	(0, 0, 20)
6	0.000	(0, 0, 25)
7	0.075	(0, 0, 30)
8	0.000	(0, 0, 35)
9	0.050	(0, 0, 40)
10	0.000	(0, 0, 45)
11	0.125	(0, 0, 50)
12	0.075	(0, 0, 55)
13	0.100	(0, 0, 60)
14	0.160	(-25, 0, 1)
15	0.160	(25, 0, 1)
16	0.160	(25, 0, 1)
17	0.160	(0,-25, 1)

Table 6 Volumetric source function $C(\hat{x}_k)$ calculated according to solidification-boundary constraint conditions given in Table 1, where Δl = (1.512/60) mm, $x_k = y_k = 0.0$ for k = 1 to 12 and $z_k = 1$ for k = 13 to 16 (WELD 3).

k	C_k	(x_k y_k z_k) (Δl)
1	0.000	(0, 0, 1)
2	0.000	(0, 0, 5)
3	0.000	(0, 0, 10)
4	0.000	(0, 0, 15)
5	0.033	(0, 0, 20)
6	0.000	(0, 0, 25)
7	0.050	(0, 0, 30)
8	0.000	(0, 0, 35)
9	0.066	(0, 0, 40)
10	0.000	(0, 0, 45)
11	0.462	(0, 0, 50)
12	0.231	(0, 0, 55)
13	0.180	(-25, 0, 1)
14	0.180	(25, 0, 1)
15	0.180	(25, 0, 1)
16	0.180	(0,-25, 1)

Table 7 Volumetric source function $C(\hat{x}_k)$ calculated according to transformation-boundary constraint conditions given in Table 1, where Δl = (1.512/60) mm, $x_k = y_k = 0.0$ for k = 1 to 11 and $z_k = 1$ for k = 12 to 15 (WELD 3).

k	C_k	(x_k y_k z_k) (Δl)
1	0.000	(0, 0, 1)
2	0.000	(0, 0, 5)
3	0.000	(0, 0, 10)
4	0.000	(0, 0, 15)
5	0.030	(0, 0, 20)
6	0.000	(0, 0, 25)
7	0.045	(0, 0, 30)
8	0.000	(0, 0, 35)
9	0.060	(0, 0, 40)
10	0.000	(0, 0, 45)
11	0.360	(0, 0, 50)
12	0.160	(-25, 0, 1)
13	0.160	(25, 0, 1)
14	0.160	(25, 0, 1)
15	0.160	(0,-25, 1)

Table 8 Volumetric source function $C(\hat{x}_k)$ calculated according to solidification-boundary constraint conditions given in Table 1, where Δl = (3.0/60) mm, $x_k = y_k = 0.0$ for k = 1 to 10 and $z_k = 1$ for k = 11 to 14 (WELD 4).

k	C_k	(x_k y_k z_k) (Δl)
1	0.000	(0, 0, 1)
2	0.000	(0, 0, 5)
3	0.186	(0, 0, 10)
4	0.000	(0, 0, 15)
5	0.186	(0, 0, 20)
6	0.000	(0, 0, 25)
7	0.186	(0, 0, 30)
8	0.372	(0, 0, 35)
9	0.651	(0, 0, 40)
10	0.651	(0, 0, 45)
11	0.650	(-25, 0, 1)
12	0.650	(25, 0, 1)
13	0.650	(25, 0, 1)
14	0.650	(0,-25, 1)

Table 9 Volumetric source function $C(\hat{x}_k)$ calculated according to transformation-boundary constraint conditions given in Table 1, where Δl = (3.0/60) mm, $x_k = y_k = 0.0$ for k = 1 to 7 and z_k = 1 for k = 8 to 11 (WELD 4).

k	C_k	(x_k y_k z_k) (Δl)
1	0.000	(0, 0, 1)
2	0.000	(0, 0, 5)
3	0.162	(0, 0, 10)
4	0.000	(0, 0, 15)
5	0.170	(0, 0, 20)
6	0.000	(0, 0, 25)
7	0.567	(0, 0, 30)
8	0.300	(-25, 0, 1)
9	0.300	(25, 0, 1)
10	0.300	(25, 0, 1)
11	0.300	(0,-25, 1)

Table 10 Volumetric source function $C(\hat{x}_k)$ calculated according to solidification-boundary constraint conditions given in Table 1, where Δl = (3.0/60) mm, $x_k = y_k = 0.0$ for k = 1 to 11 (WELD 5).

k	C_k	(x_k y_k z_k) (Δl)
1	1.037	(0, 0, 1)
2	0.000	(0, 0, 5)
3	0.415	(0, 0, 10)
4	0.000	(0, 0, 15)
5	0.484	(0, 0, 20)
6	0.000	(0, 0, 25)
7	0.484	(0, 0, 30)
8	0.138	(0, 0, 35)
9	0.553	(0, 0, 40)
10	0.000	(0, 0, 45)
11	0.967	(0, 0, 50)

Table 11 Volumetric source function $C(\hat{x}_k)$ calculated according to transformation-boundary constraint conditions given in Table 1, where Δl = (3.0/60) mm, $x_k = y_k = 0.0$ for k = 1 to 11 (WELD 5).

k	C_k	(x_k y_k z_k) (Δl)
1	1.037	(0, 0, 1)
2	0.000	(0, 0, 5)
3	0.366	(0, 0, 10)
4	0.000	(0, 0, 15)
5	0.427	(0, 0, 20)
6	0.000	(0, 0, 25)
7	0.366	(0, 0, 30)
8	0.000	(0, 0, 35)
9	0.305	(0, 0, 40)
10	0.000	(0, 0, 45)
11	0.439	(0, 0, 50)

Table 12 Volumetric source function $C(\hat{x}_k)$ calculated according to solidification-boundary constraint conditions given in Table 1, where Δl = (3.0/60) mm (WELD 6).

k	C_k	(x_k y_k z_k) (Δl)
1	1.065	(0, 0, 1)
2	0.000	(0, 0, 5)
3	0.568	(0, 0, 10)
4	0.000	(0, 0, 15)
5	0.568	(0, 0, 20)
6	0.000	(0, 0, 25)
7	0.568	(0, 0, 30)
8	0.000	(0, 0, 35)
9	0.568	(0, 0, 40)
10	0.000	(0, 0, 45)
11	0.568	(0, 0, 50)
12	0.000	(0, 0, 55)
13	0.355	(0, 0, 60)

Table 13 Volumetric source function $C(\hat{x}_k)$ calculated according to transformation-boundary constraint conditions given in Table 1, where Δl = (3.0/60) mm (WELD 6).

k	C_k	(x_k y_k z_k) (Δl)
1	0.928	(0, 0, 1)
2	0.000	(0, 0, 5)
3	0.464	(0, 0, 10)
4	0.000	(0, 0, 15)
5	0.464	(0, 0, 20)
6	0.000	(0, 0, 25)
7	0.464	(0, 0, 30)
8	0.000	(0, 0, 35)
9	0.348	(0, 0, 40)
10	0.000	(0, 0, 45)
11	0.290	(0, 0, 50)
12	0.000	(0, 0, 55)
13	0.290	(0, 0, 60)

Table 14 Volumetric source function $C(\hat{x}_k)$ calculated according to solidification-boundary constraint conditions given in Table 1, where Δl = (3.0/60) mm, $x_k = y_k = 0.0$ for k = 1 to 11 (WELD 7).

k	C_k	(x_k y_k z_k) (Δl)
1	1.119	(0, 0, 1)
2	0.000	(0, 0, 5)
3	0.522	(0, 0, 10)
4	0.000	(0, 0, 15)
5	0.373	(0, 0, 20)
6	0.000	(0, 0, 25)
7	0.522	(0, 0, 30)
8	0.000	(0, 0, 35)
9	0.522	(0, 0, 40)
10	0.298	(0, 0, 45)
11	0.821	(0, 0, 50)

Table 15 Volumetric source function $C(\hat{x}_k)$ calculated according to transformation-boundary constraint conditions given in Table 1, where Δl = (3.0/60) mm (WELD 7).

k	C_k	(x_k y_k z_k) (Δl)
1	1.173	(0, 0, 1)
2	0.000	(0, 0, 5)
3	0.483	(0, 0, 10)
4	0.000	(0, 0, 15)
5	0.345	(0, 0, 20)
6	0.000	(0, 0, 25)
7	0.483	(0, 0, 30)
8	0.000	(0, 0, 35)
9	0.414	(0, 0, 40)
10	0.000	(0, 0, 45)
11	0.490	(0, 0, 50)

Table 16 Volumetric source function $C(\hat{x}_k)$ calculated according to solidification-boundary constraint conditions given in Table 1, where Δl = (3.0/60) mm (WELD 8).

k	C_k	(x_k y_k z_k) (Δl)
1	0.000	(0, 0, 1)
2	0.000	(0, 0, 5)
3	0.132	(0, 0, 10)
4	0.000	(0, 0, 15)
5	0.132	(0, 0, 20)
6	0.000	(0, 0, 25)
7	0.660	(0, 0, 30)
8	0.000	(0, 0, 35)
9	0.825	(0, 0, 40)
10	0.000	(0, 0, 45)
11	0.660	(0, 0, 50)
12	0.550	(-20, 0, 1)
13	0.550	(20, 0, 1)
14	0.550	(0,-20, 1)
15	0.550	(0, 20, 1)

Table 17 Volumetric source function $C(\hat{x}_k)$ calculated according to transformation-boundary constraint conditions given in Table 1, where Δl = (3.0/60) mm (WELD 8).

k	C_k	(x_k y_k z_k) (Δl)
1	0.000	(0, 0, 1)
2	0.000	(0, 0, 5)
3	0.116	(0, 0, 10)
4	0.000	(0, 0, 15)
5	0.116	(0, 0, 20)
6	0.000	(0, 0, 25)
7	0.638	(0, 0, 30)
8	0.000	(0, 0, 35)
9	0.522	(0, 0, 40)
10	0.000	(0, 0, 45)
11	0.406	(0, 0, 50)
12	0.500	(-20, 0, 1)
13	0.500	(20, 0, 1)
14	0.500	(0,-20, 1)
15	0.500	(0, 20, 1)

Table 18 Volumetric source function $C(\hat{x}_k)$ calculated according to solidification-boundary constraint conditions given in Table 1, where Δl = (3.0/60) mm (WELD 9).

k	C_k	(x_k y_k z_k) (Δl)
1	0.000	(0, 0, 1)
2	0.000	(0, 0, 5)
3	0.136	(0, 0, 10)
4	0.000	(0, 0, 15)
5	0.136	(0, 0, 20)
6	0.000	(0, 0, 25)
7	0.136	(0, 0, 30)
8	0.000	(0, 0, 35)
9	1.020	(0, 0, 40)
10	0.340	(0, 0, 45)
11	0.580	(-20, 0, 1)
12	0.580	(20, 0, 1)
13	0.580	(0,-20, 1)
14	0.580	(0, 20, 1)

Table 19 Volumetric source function $C(\hat{x}_k)$ calculated according to transformation-boundary constraint conditions given in Table 1, where Δl = (3.0/60) mm (WELD 9)

k	C_k	(x_k y_k z_k) (Δl)
1	0.000	(0, 0, 1)
2	0.000	(0, 0, 5)
3	0.000	(0, 0, 10)
4	0.116	(0, 0, 15)
5	0.000	(0, 0, 20)
6	0.116	(0, 0, 25)
7	0.406	(0, 0, 30)
8	0.348	(0, 0, 35)
9	0.348	(0, 0, 40)
10	0.580	(-20, 0, 1)
11	0.580	(20, 0, 1)
12	0.580	(0,-20, 1)
13	0.580	(0, 20, 1)

.

Table 20 Volumetric source function $C(\hat{x}_k)$ calculated according to solidification-boundary constraint conditions given in Table 1, where Δl = (3.0/60) mm (WELD 10).

k	C_k	(x_k y_k z_k) (Δl)
1	0.000	(0, 0, 1)
2	0.000	(0, 0, 5)
3	0.560	(0, 0, 10)
4	0.000	(0, 0, 15)
5	0.560	(0, 0, 20)
6	0.000	(0, 0, 25)
7	0.560	(0, 0, 30)
8	0.000	(0, 0, 35)
9	0.560	(0, 0, 40)
10	0.000	(0, 0, 45)
11	0.448	(0, 0, 50)
12	0.000	(0, 0, 55)
13	0.392	(0, 0, 60)
14	0.400	(-20, 0, 1)
15	0.400	(20, 0, 1)
16	0.400	(0,-20, 1)
17	0.400	(0, 20, 1)

Table 21 Volumetric source function $C(\hat{x}_k)$ calculated according to transformation-boundary constraint conditions given in Table 1, where Δl = (3.0/60) mm, $x_k = y_k = 0.0$ for k = 1 to 13 and $z_k = 1$ for k = 14 to 17 (WELD 10).

k	C_k	(x_k y_k z_k) (Δl)
1	0.000	(0, 0, 1)
2	0.000	(0, 0, 5)
3	0.530	(0, 0, 10)
4	0.000	(0, 0, 15)
5	0.530	(0, 0, 20)
6	0.000	(0, 0, 25)
7	0.530	(0, 0, 30)
8	0.000	(0, 0, 35)
9	0.530	(0, 0, 40)
10	0.000	(0, 0, 45)
11	0.318	(0, 0, 50)
12	0.000	(0, 0, 55)
13	0.212	(0, 0, 60)
14	0.360	(-20, 0, 1)
15	0.360	(20, 0, 1)
16	0.360	(0,-20, 1)
17	0.360	(0, 20, 1)

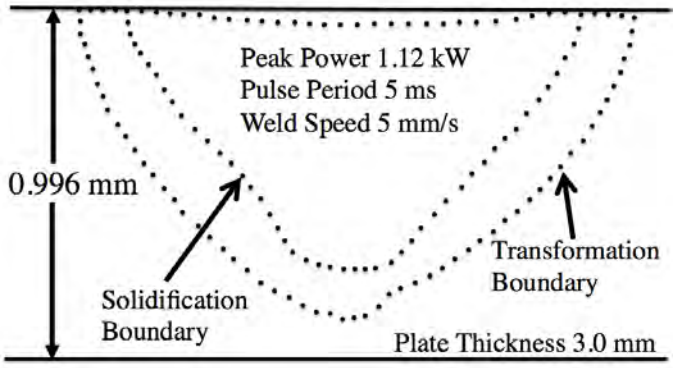

Fig. 2 Experimentally measured transverse weld cross sections of solidification and transformation boundaries (WELD 1).

.

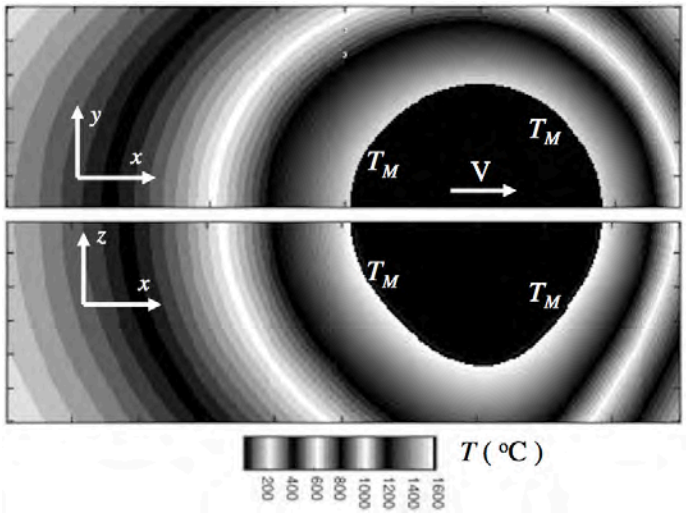

Fig. 3 Two-dimensional slices, at half workpiece top surface and longitudinal cross section at symmetry plane, of three-dimensional temperature field (^{o}C) calculated using cross section information given in Table 1 for solidification boundary (WELD 1).

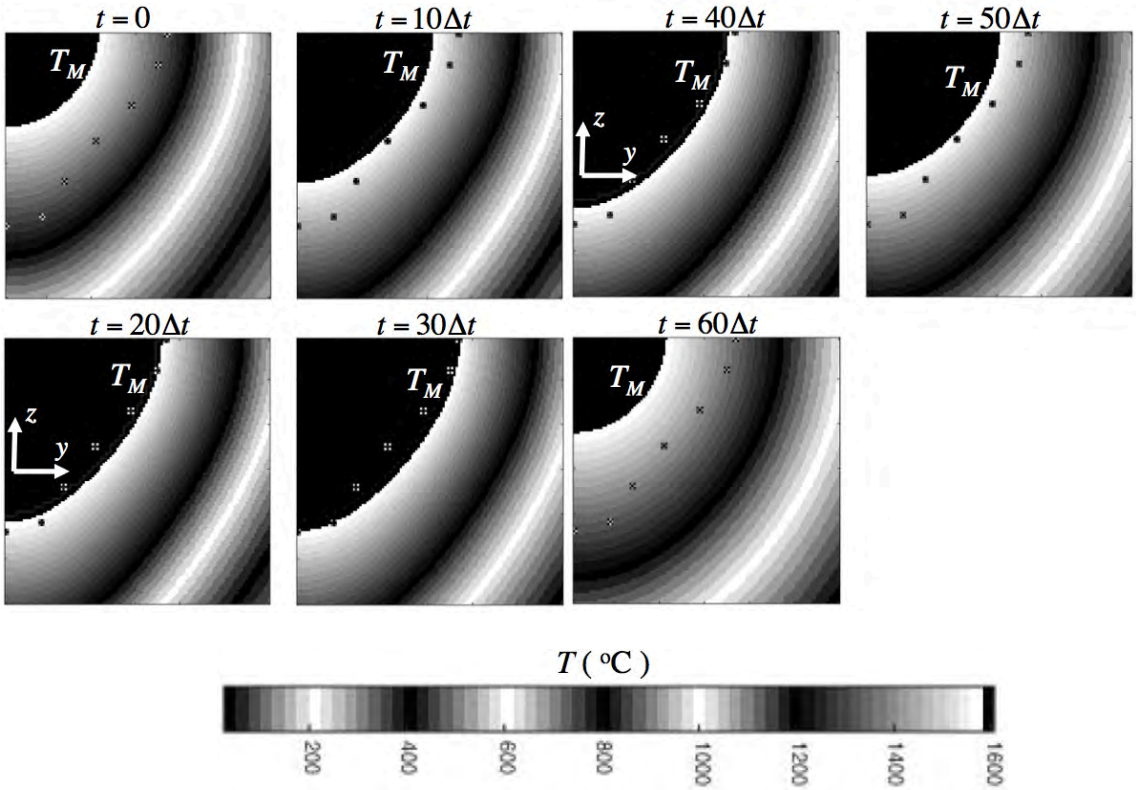

Fig. 4 Temperature history (^{o}C) of transverse cross section of weld calculated using cross section information given in Table 1 for solidification boundary, where $\Delta t = \Delta l$ /V, Δl = (0.996/60) mm and V = 5.0 mm/s (WELD 1).

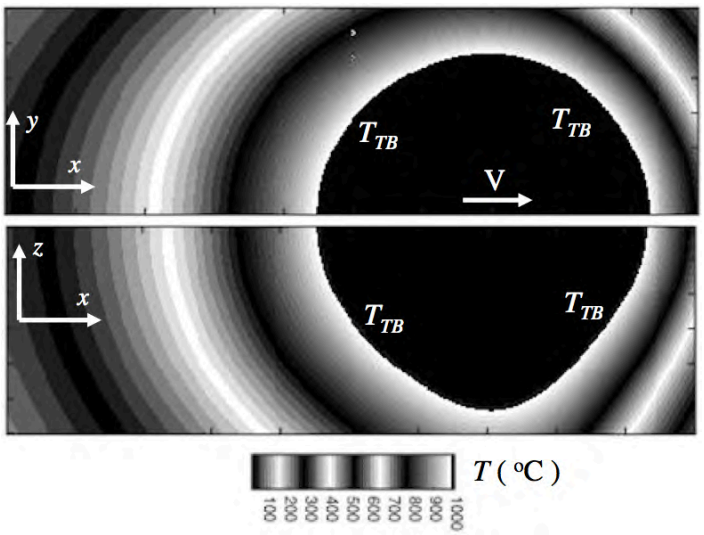

Fig. 5 Two-dimensional slices, at half workpiece top surface and longitudinal cross section at symmetry plane, of three-dimensional temperature field (^{o}C) calculated using cross section information given in Table 1 for transformation boundary (WELD 1).

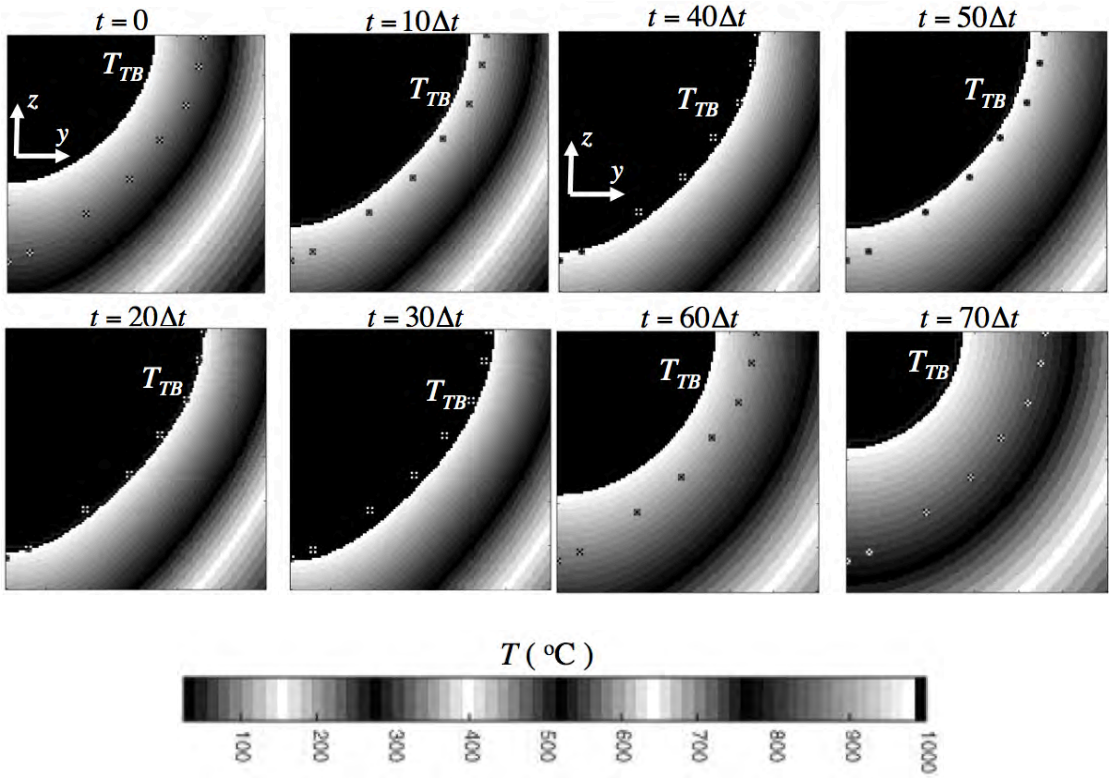

Fig. 6 Temperature history (^{o}C) of transverse cross section of weld calculated using cross section information given in Table 1 for transformation boundary, where $\Delta t = \Delta l / V$, Δl = (0.996/60) mm and V = 5.0 mm/s (WELD 1).

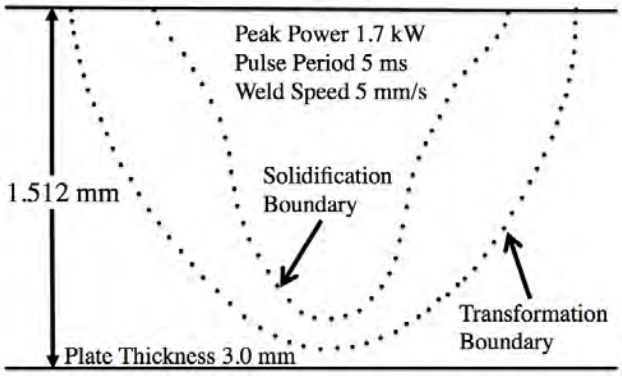

Fig. 7 Experimentally measured transverse weld cross sections of solidification and transformation boundaries (WELD 3).

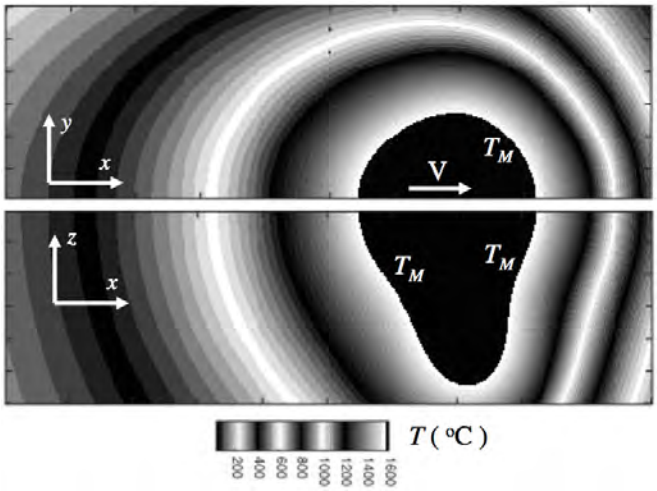

Fig. 8 Two-dimensional slices, at half workpiece top surface and longitudinal cross section at symmetry plane, of three-dimensional temperature field (^{o}C) calculated using cross section information given in Table 1 for solidification boundary (WELD 3).

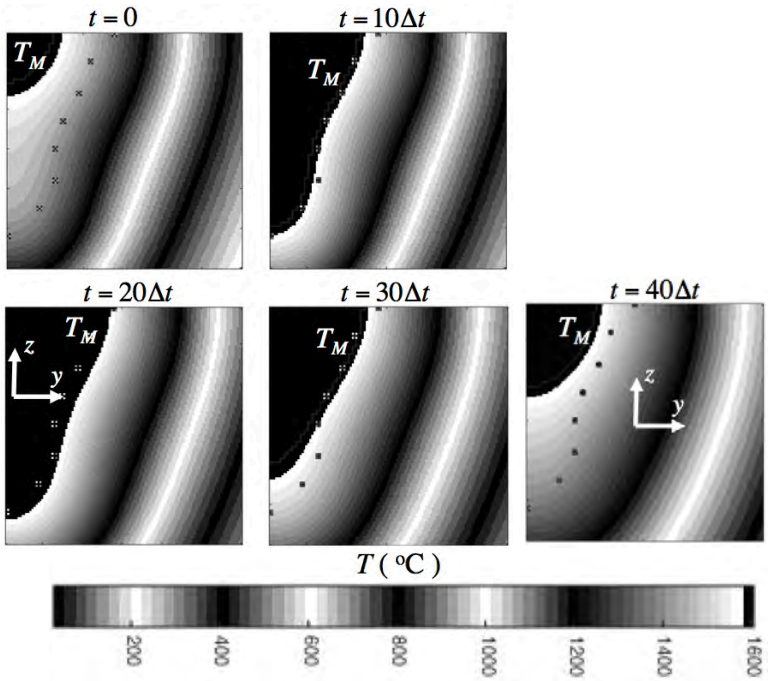

Fig. 9 Temperature history (°C) of transverse cross section of weld calculated using cross section information given in Table 1 for solidification boundary, where $\Delta t = \Delta l / V$, Δl = (1.512/60) mm and V = 5.0 mm/s (WELD 3).

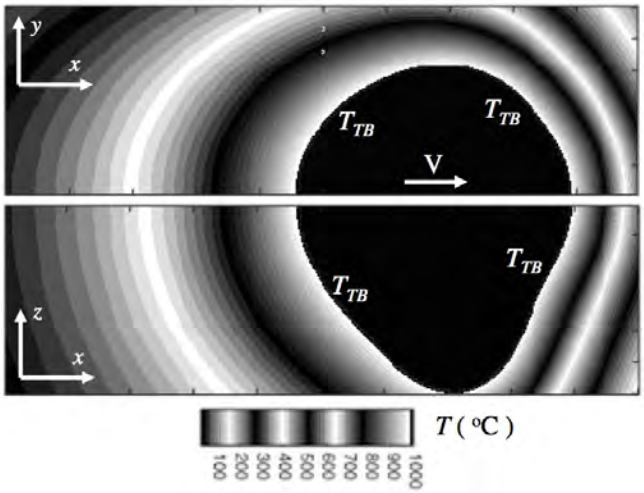

Fig. 10 Two-dimensional slices, at half workpiece top surface and longitudinal cross section at symmetry plane, of three-dimensional temperature field (°C) calculated using cross section information given in Table 1 for transformation boundary (WELD 3).

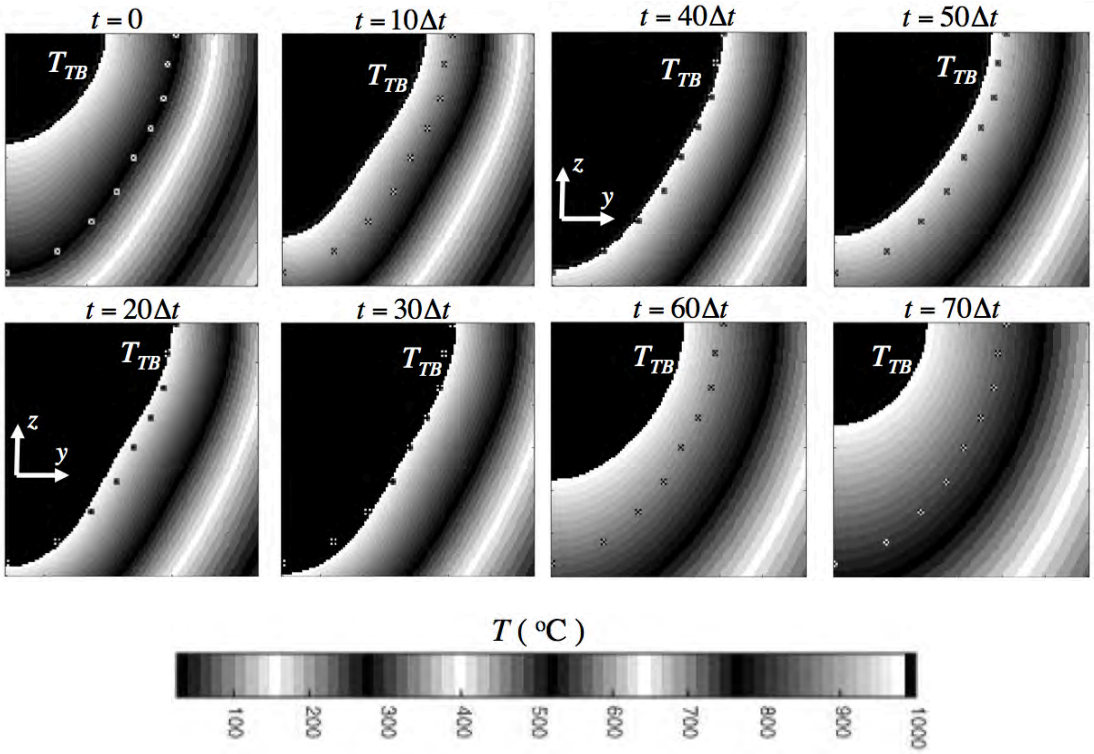

Fig. 11 Temperature history (^{o}C) of transverse cross section of weld calculated using cross section information given in Table 1 for transformation boundary, where $\Delta t = \Delta l$ /V, Δl = (1.512/60) mm and V = 5.0 mm/s (WELD 3).

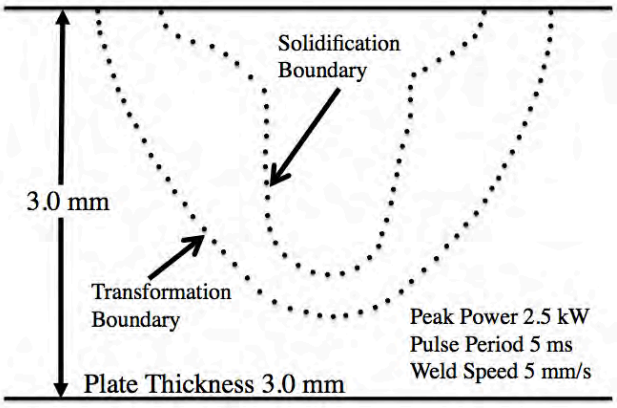

Fig. 12 Experimentally measured transverse weld cross sections of solidification and transformation boundaries (WELD 4).

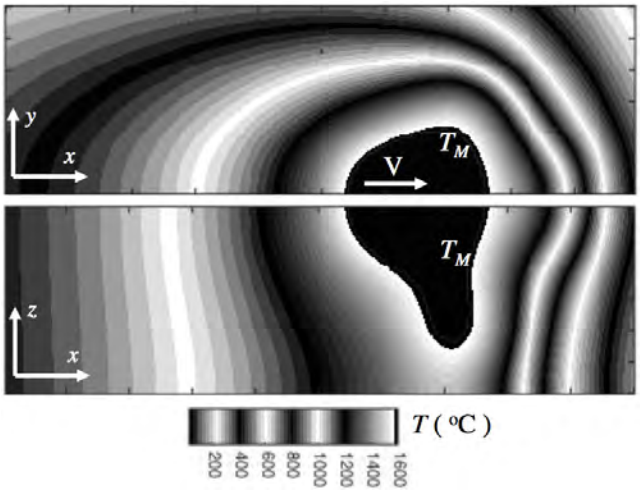

Fig. 13 Two-dimensional slices, at half workpiece top surface and longitudinal cross section at symmetry plane, of three-dimensional temperature field (^{o}C) calculated using cross section information given in Table 1 for solidification boundary (WELD 4).

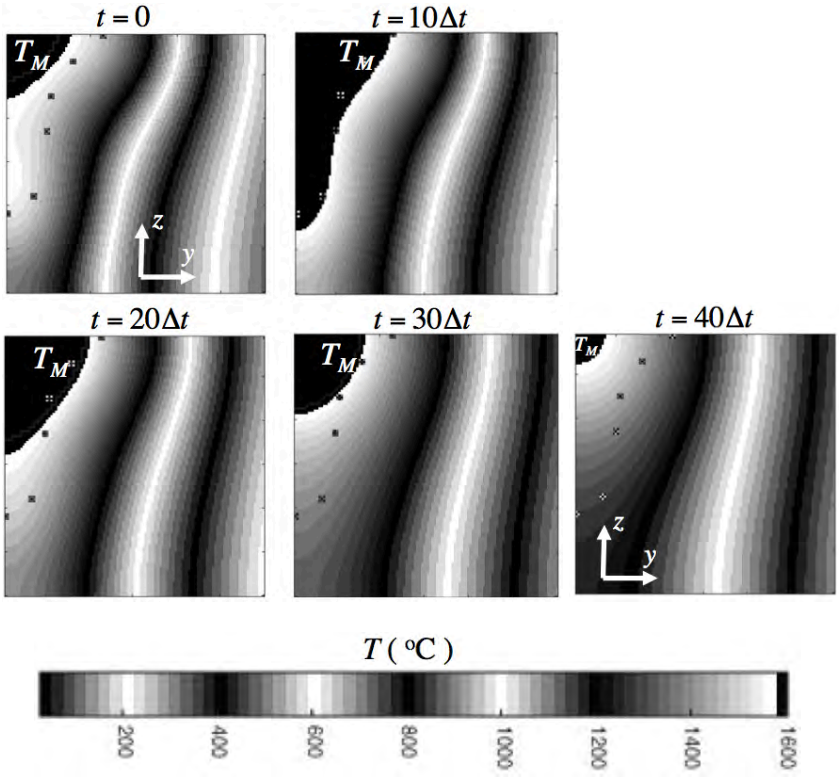

Fig. 14 Temperature history (^{o}C) of transverse cross section of weld calculated using cross section information given in Table 1 for solidification boundary, where $\Delta t = \Delta l$ /V, Δl = (3.0/60) mm and V = 5.0 mm/s (WELD 4).

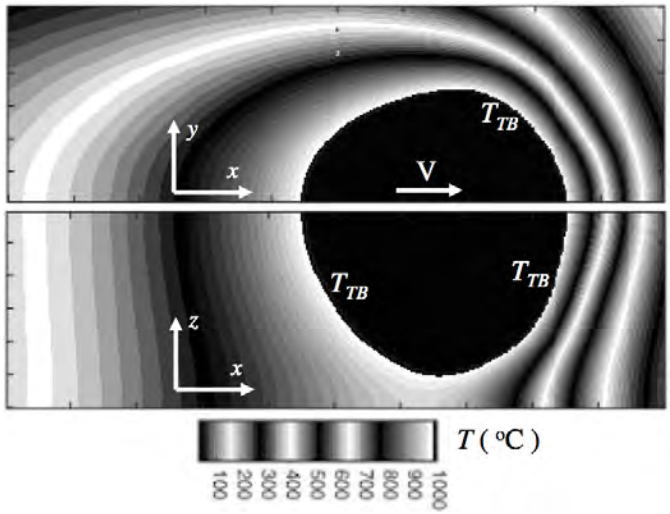

Fig. 15 Two-dimensional slices, at half workpiece top surface and longitudinal cross section at symmetry plane, of three-dimensional temperature field (°C) calculated using cross section information given in Table 1 for transformation boundary (WELD 4).

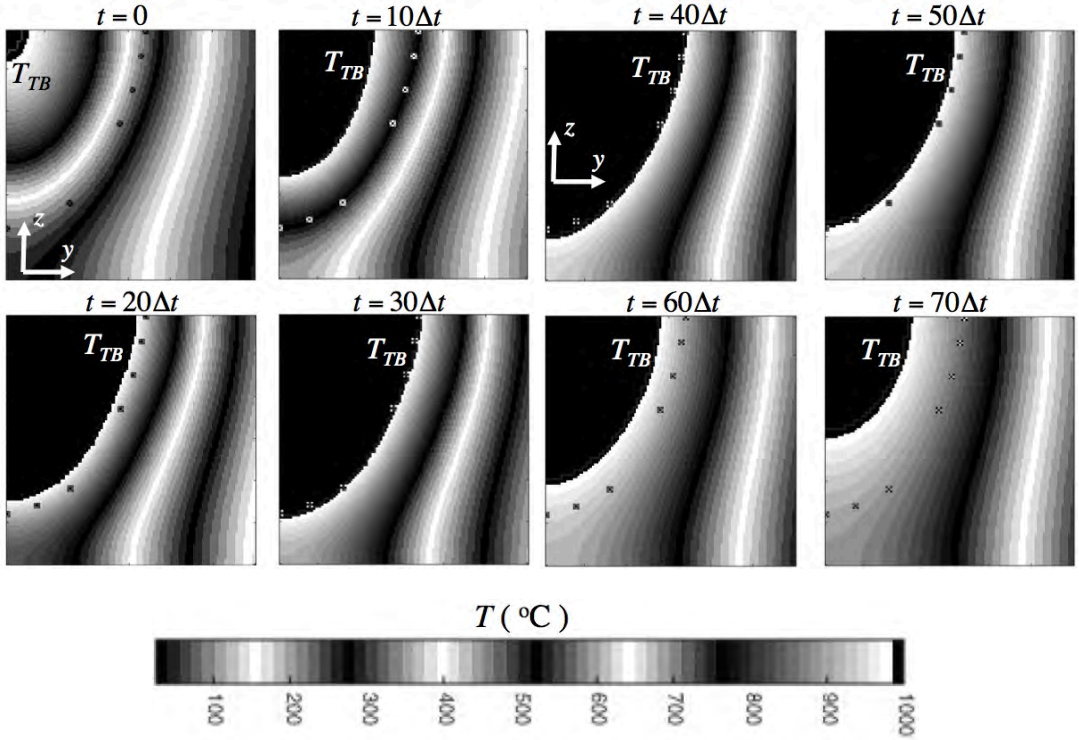

Fig. 16 Temperature history (°C) of transverse cross section of weld calculated using cross section information given in Table 1 for transformation boundary, where $\Delta t = \Delta l$ /V, Δl = (3.0/60) mm and V = 5.0 mm/s (WELD 4).

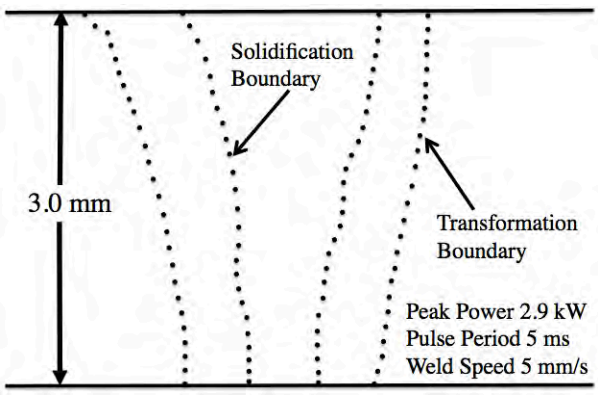

Fig. 17 Experimentally measured transverse weld cross sections of solidification and transformation boundaries (WELD 6).

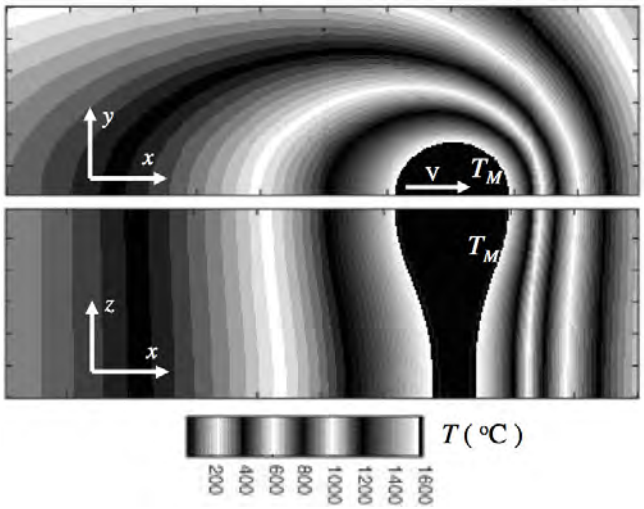

Fig. 18 Two-dimensional slices, at half workpiece top surface and longitudinal cross section at symmetry plane, of three-dimensional temperature field (^{o}C) calculated using cross section information given in Table 1 for solidification boundary (WELD 6).

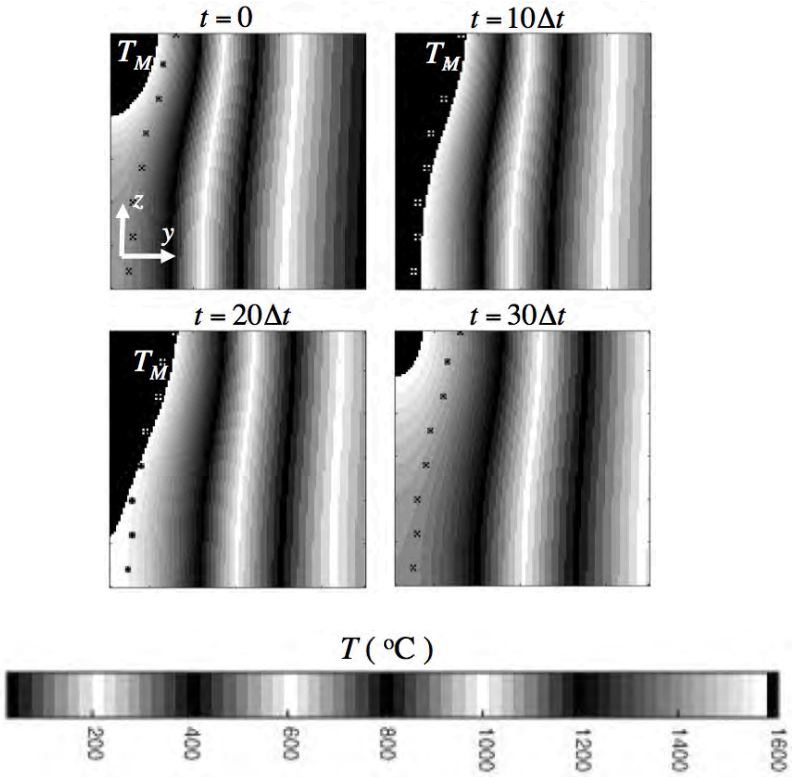

Fig. 19 Temperature history (°C) of transverse cross section of weld calculated using cross section information given in Table 1 for solidification boundary, where $\Delta t = \Delta l / V$, Δl = (3.0/60) mm and V = 5.0 mm/s (WELD 6).

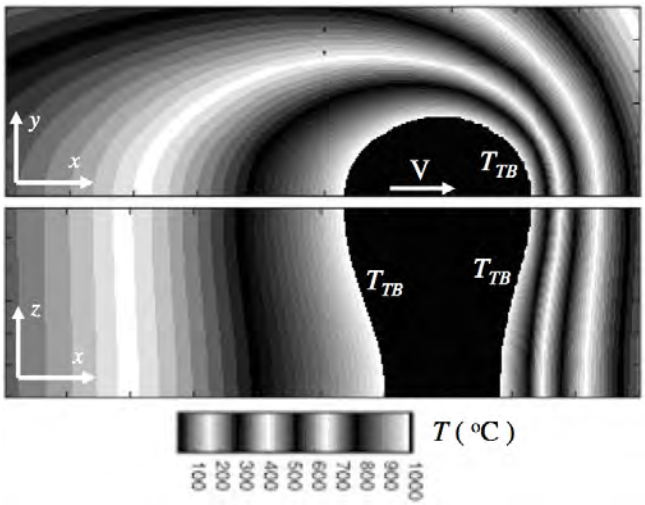

Fig. 20 Two-dimensional slices, at half workpiece top surface and longitudinal cross section at symmetry plane, of three-dimensional temperature field (°C) calculated using cross section information given in Table 1 for transformation boundary (WELD 6).

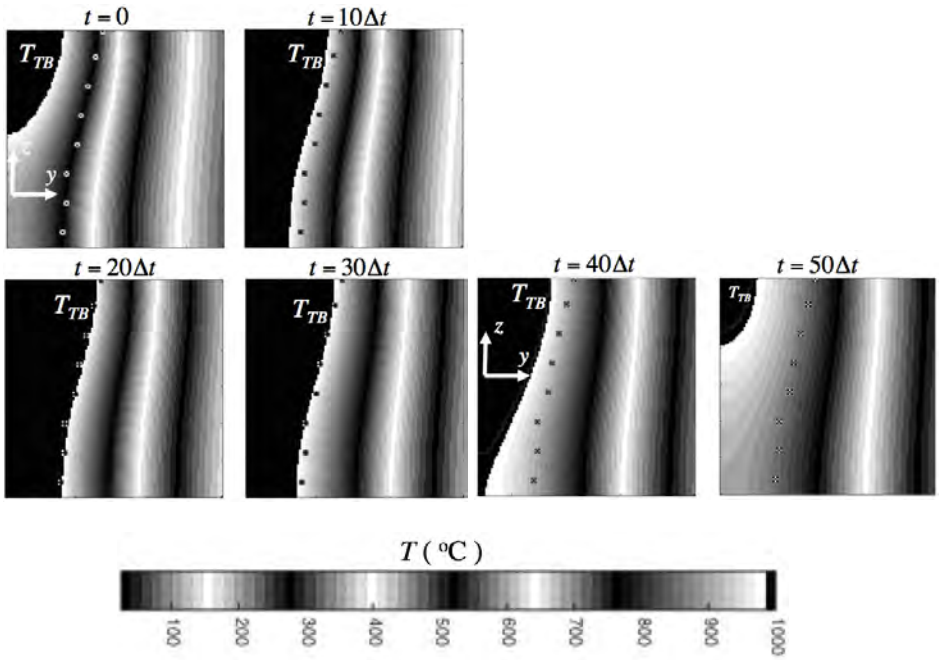

Fig. 21 Temperature history (^{o}C) of transverse cross section of weld calculated using cross section information given in Table 1 for transformation boundary, where $\Delta t = \Delta l$ /V, Δl = (3.0/60) mm and V = 5.0 mm/s (WELD 6).

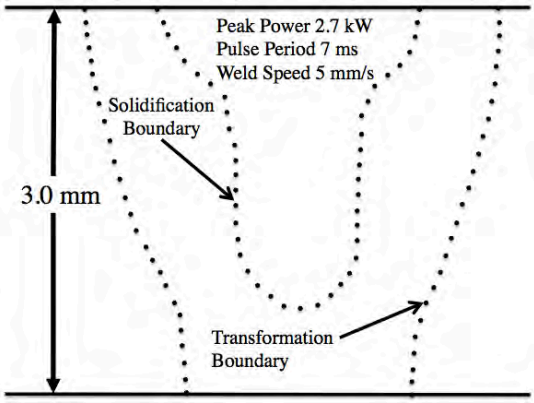

Fig. 22 Experimentally measured transverse weld cross sections of solidification and transformation boundaries (WELD 8).

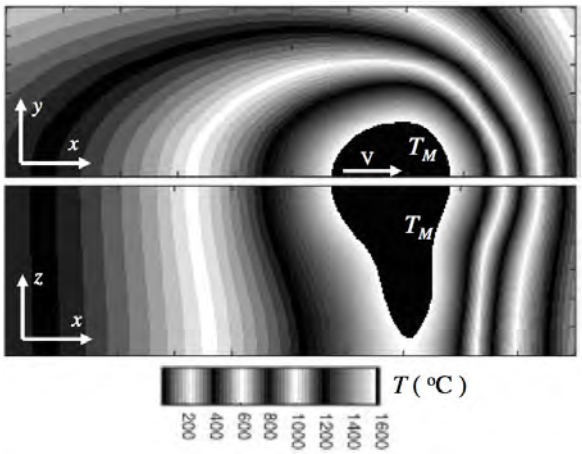

Fig. 23 Two-dimensional slices, at half workpiece top surface and longitudinal cross section at symmetry plane, of three-dimensional temperature field (°C) calculated using cross section information given in Table 1 for solidification boundary (WELD 8).

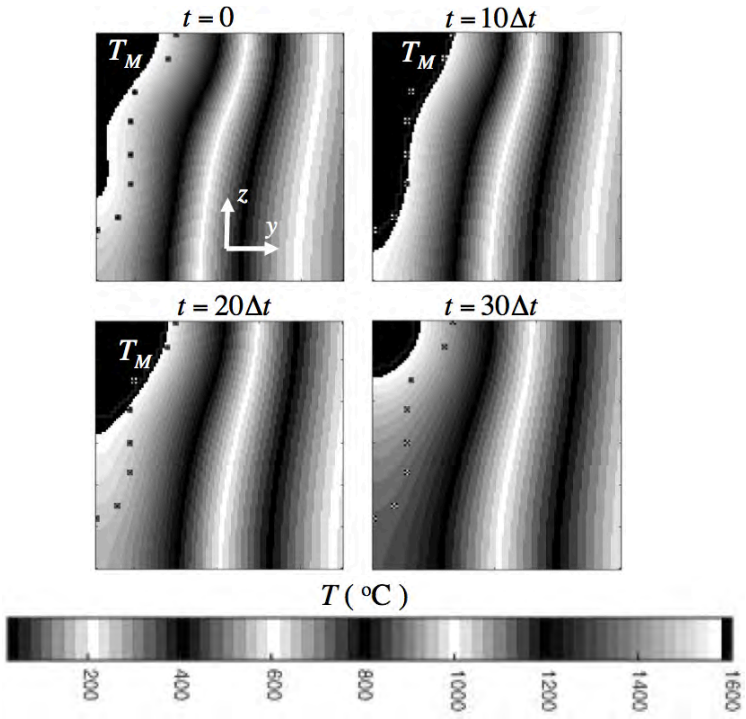

Fig. 24 Temperature history (°C) of transverse cross section of weld calculated using cross section information given in Table 1 for solidification boundary, where $\Delta t = \Delta l$ /V, Δl = (3.0/60) mm and V = 5.0 mm/s (WELD 8).

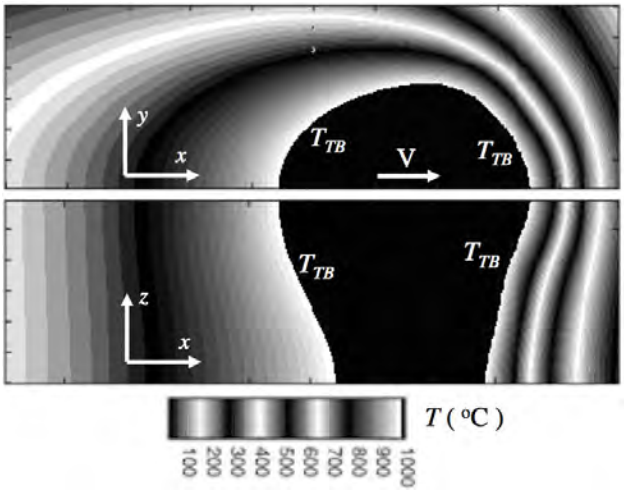

Fig. 25 Two-dimensional slices, at half workpiece top surface and longitudinal cross section at symmetry plane, of three-dimensional temperature field (^{o}C) calculated using cross section information given in Table 1 for transformation boundary (WELD 8).

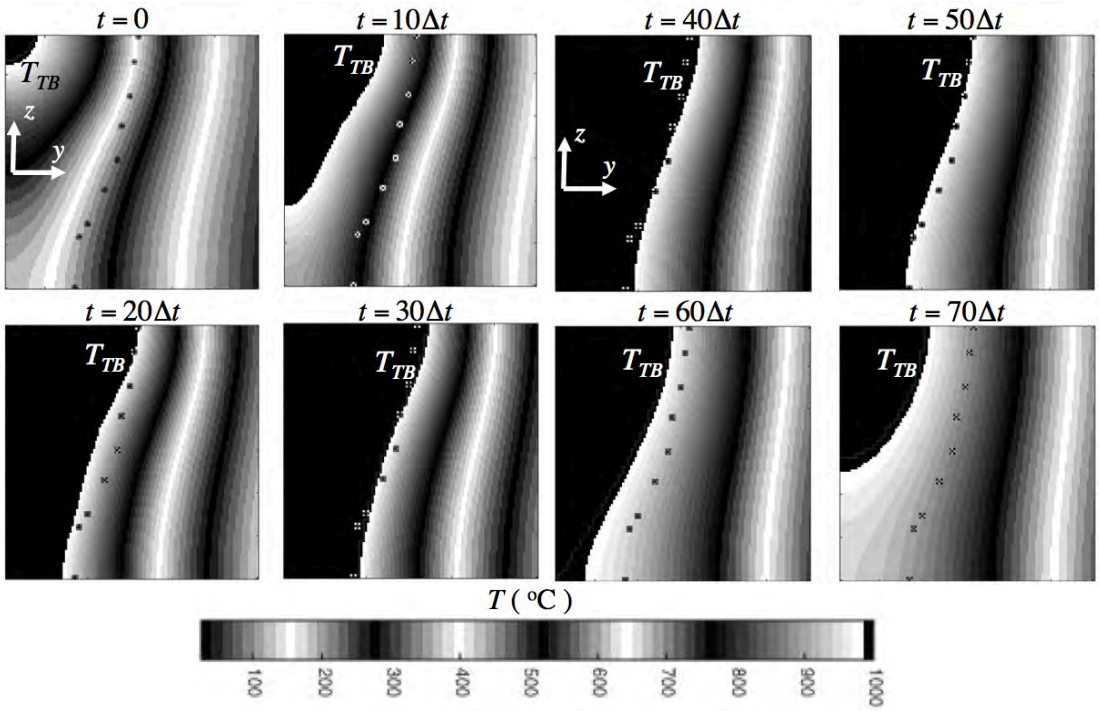

Fig. 26 Temperature history (^{o}C) of transverse cross section of weld calculated using cross section information given in Table 1 for transformation boundary, where $\Delta t = \Delta l$ /V, Δl = (3.0/60) mm and V = 5.0 mm/s (WELD 8).

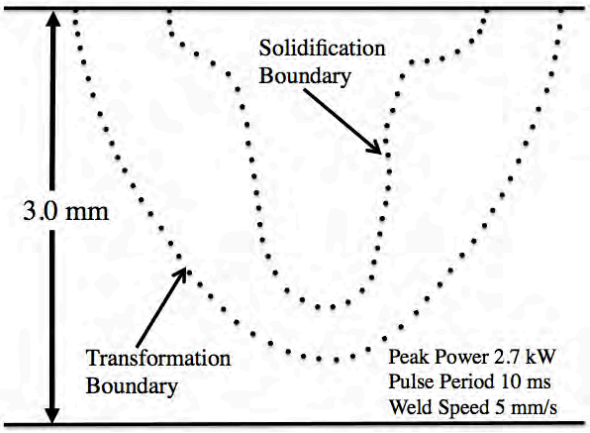

Fig. 27 Experimentally measured transverse weld cross sections of solidification and transformation boundaries (WELD 9).

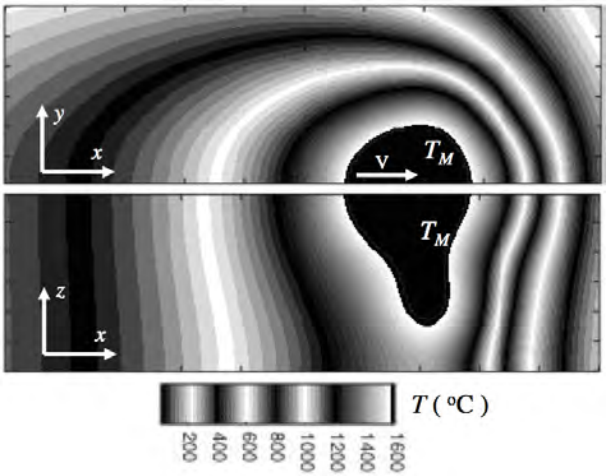

Fig. 28 Two-dimensional slices, at half workpiece top surface and longitudinal cross section at symmetry plane, of three-dimensional temperature field (^{o}C) calculated using cross section information given in Table 1 for solidification boundary (WELD 9).

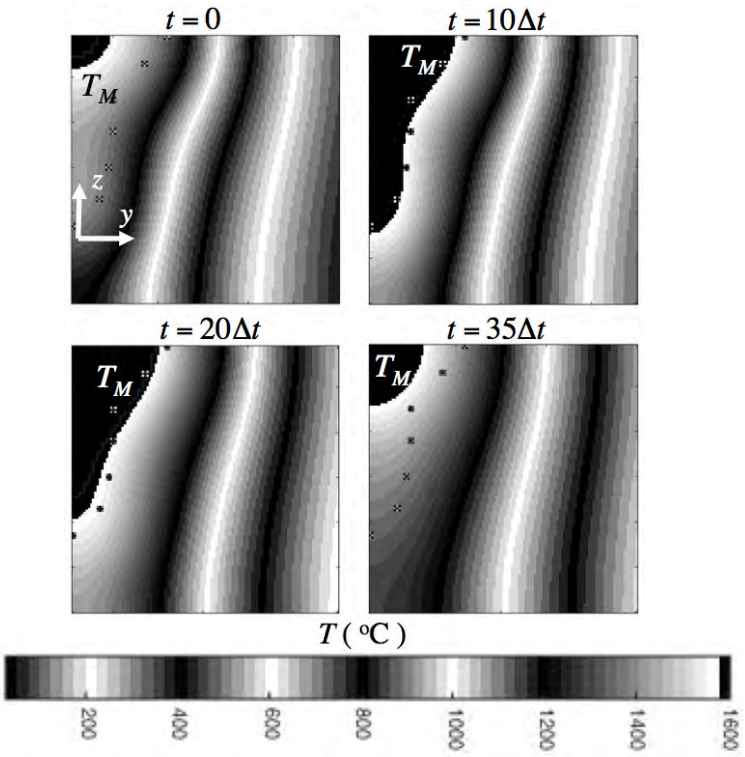

Fig. 29 Temperature history (°C) of transverse cross section of weld calculated using cross section information given in Table 1 for solidification boundary, where $\Delta t = \Delta l$ /V, Δl = (3.0/60) mm and V = 5.0 mm/s (WELD 9).

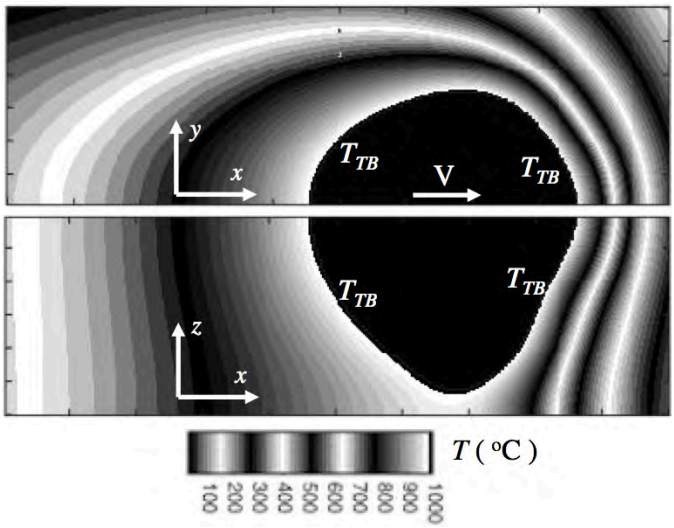

Fig. 30 Two-dimensional slices, at half workpiece top surface and longitudinal cross section at symmetry plane, of three-dimensional temperature field (°C) calculated using cross section information given in Table 1 for transformation boundary (WELD 9).

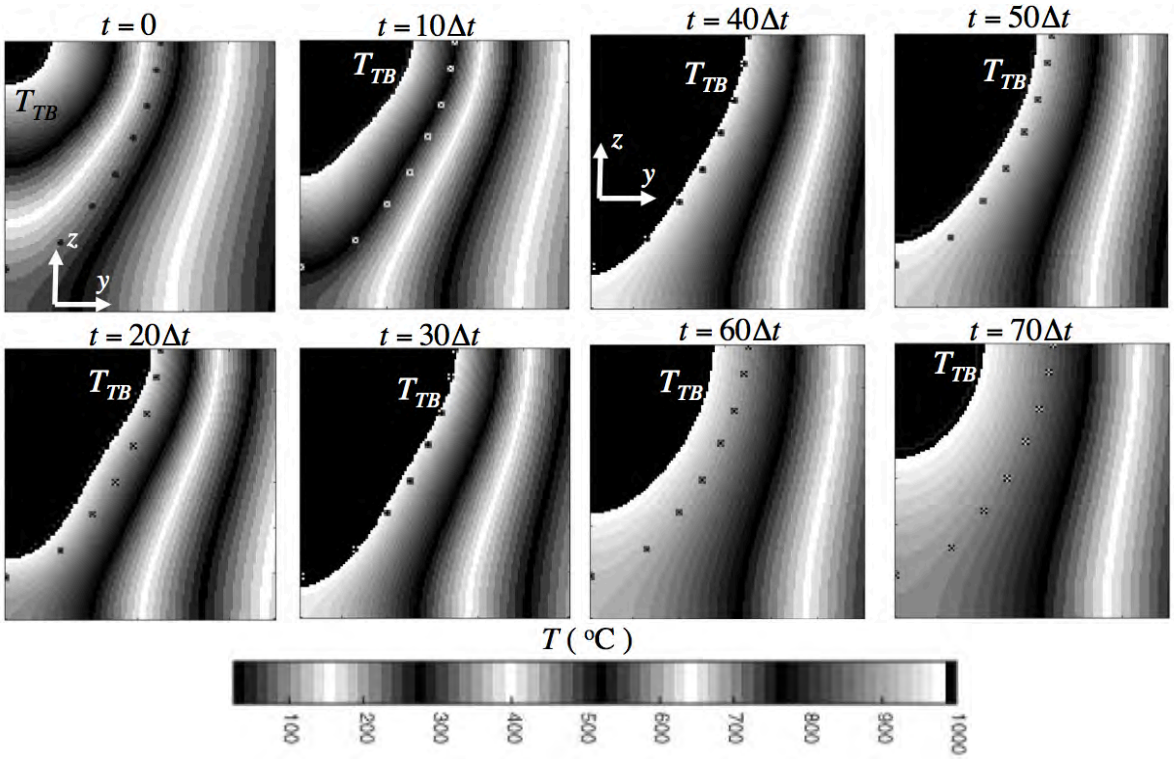

Fig. 31 Temperature history (^{o}C) of transverse cross section of weld calculated using cross section information given in Table 1 for transformation boundary, where $\Delta t = \Delta l$ /V, Δl = (3.0/60) mm and V = 5.0 mm/s (WELD 9).

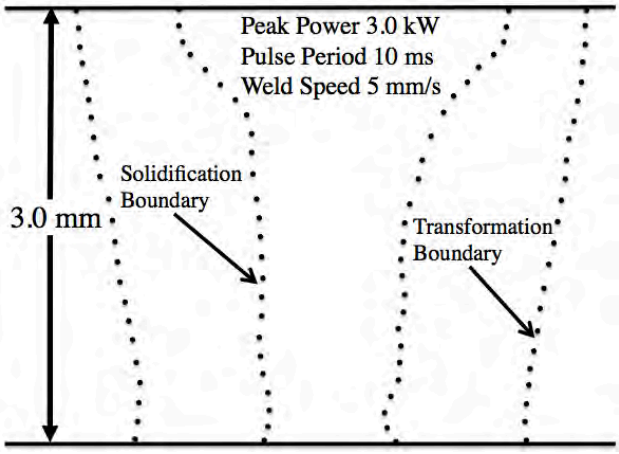

Fig. 32 Experimentally measured transverse weld cross sections of solidification and transformation boundaries (WELD 10).

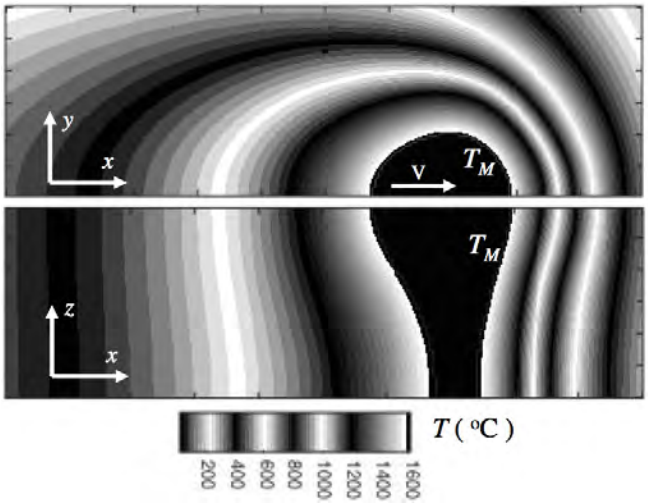

Fig. 33 Two-dimensional slices, at half workpiece top surface and longitudinal cross section at symmetry plane, of three-dimensional temperature field (°C) calculated using cross section information given in Table 1 for solidification boundary (WELD 10).

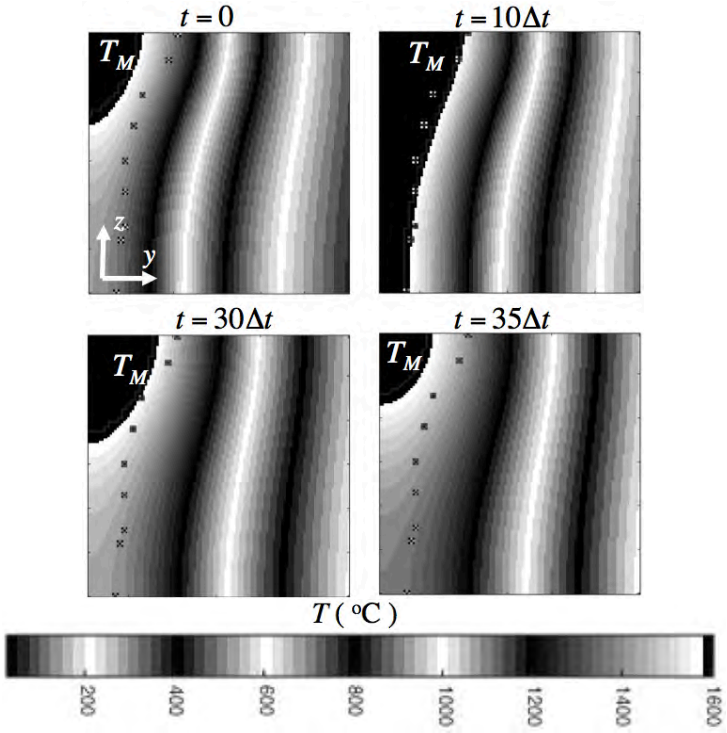

Fig. 34 Temperature history (°C) of transverse cross section of weld calculated using cross section information given in Table 1 for solidification boundary, where $\Delta t = \Delta l$ /V, Δl = (3.0/60) mm and V = 5.0 mm/s (WELD 10).

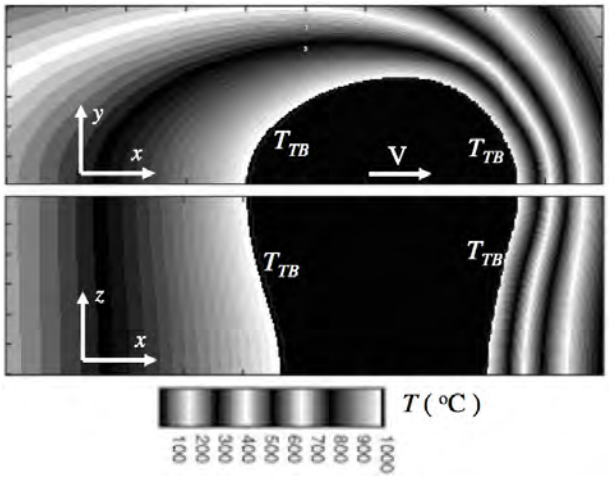

Fig. 35 Two-dimensional slices, at half workpiece top surface and longitudinal cross section at symmetry plane, of three-dimensional temperature field (°C) calculated using cross section information given in Table 1 for transformation boundary (WELD 10).

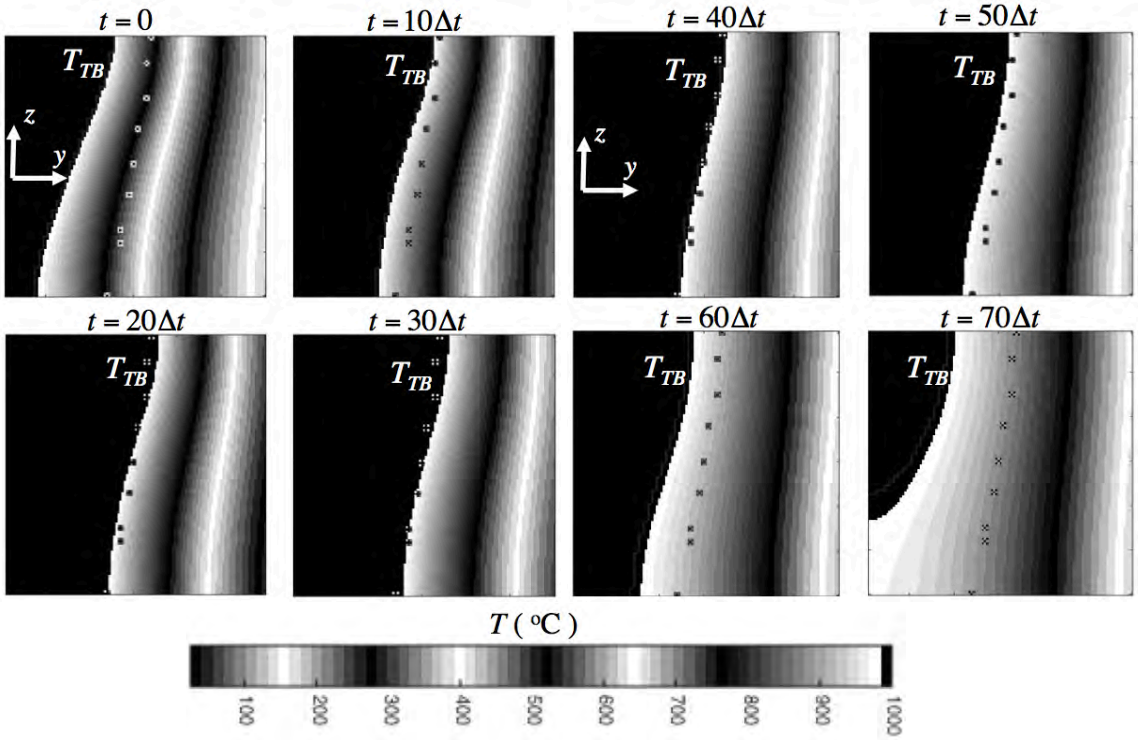

Fig. 36 Temperature history (°C) of transverse cross section of weld calculated using cross section information given in Table 1 for transformation boundary, where $\Delta t = \Delta l$ /V, Δl = (3.0/60) mm and V = 5.0 mm/s (WELD 10).

Discussion

The inverse analysis procedure entails calculating either a three-dimensional solidification or transformation boundary using experimentally measured constraint conditions, and the temperature field consistent with the isothermal surface associated with this boundary.

Shown in the above figures are two-dimensional slices of the calculated three-dimensional temperature field obtained using the constraint conditions given in Table 1 for the measured solidification and transformation boundaries, which are parallel to the relative motion of laser beam and workpiece. In addition, shown in above figures are two-dimensional slices of the three-dimensional temperature fields that are perpendicular to the relative motion of laser beam and workpiece. Referring to these figures, it should be noted that $t = 0$ has been assigned arbitrarily to a two-dimensional slice at the leading edge of the solidification or transformation boundary. Accordingly, shown in these figures is passage with time of the calculated three-dimensional solidification and transformation boundaries through experimentally measured transverse cross sections of these boundaries. Referring to the calculated temperature fields shown above, it is important to note that the constraint conditions on the calculated three-dimensional solidification and transformation boundaries are that the projections of all their two-dimenional transverse slices, as a function of time, are consistent with the experimentally measured transverse cross sections of the solidification and transformation boundaries, respectively.

The final stage of the analysis entails calculation of temperature histories as a function of transverse position within the cross section of the weld. This is accomplished by constructing a steady state three-dimensional temperature field that is consistent with experimentally measured constraint conditions for the solidification boundary or for both solidification and transformation boundaries. In cases where both the solidification and transformation boundaries are adopted as constraints, this construction combines two regions of the temperature field. One region consists of the calculated temperature field obtained using transformation boundary constraints for all temperatures less than and equal to the transformation temperature T_{TB}. The other region consists of the temperature field that is obtained by three-dimensional interpolation between isothermal surfaces T_M and T_{TB}, which are associated with the solidification and transformation boundaries, respectively. In general, the numerical procedure for interpolation between constrained isotherms is a separate issue for consideration.

Parameter optimization can in general be enhanced if there exist initial estimates of the parameter values, which require only fine adjustment with respect to constraint conditions. Parameter adjustment with respect to similar types of welds, whose process parameters are within similar regimes to those for which discrete source values $C(\hat{x}_k)$ have been determined, can adopt these values as initial estimates. Although the thermal diffusivity κ and melt temperature T_M of Ti and its different alloys may vary, this variation is not over a wide range of values. This is the case in general for different types metals and their alloys. It follows that parameter optimization for a specific type of Ti-alloy weld, which uses initial estimates of parameter values corresponding to a different type of Ti-alloy weld, can adopt κ and T_M as adjustable parameters, as well as the discrete source function $C(\hat{x}_k)$.

For this study the transformation temperature T_{TB} was given the value of 995 ^{o}C, which is assumed approximately the temperature of the α to β phase transformation for Ti-6Al-4V. In practice, the association of a specific temperature with an experimentally observed transformation boundary is within certain error limits. In particular, for welding of Ti and its alloys, there exists a range of temperatures for the phase transformation from α to β phase

during heating and then β to α during cooling. In addition, in practice the shape of the fusion boundary is extremely difficult to define for welds of Ti and its alloys in general [1]. Accordingly, the choice of a transformation temperature T_{TB} to be associated with a specific isothermal boundary, as well as the location and shape of the solidification boundary, suggests the need for sensitivity analysis of the calculated temperature field with respect changes in T_{TB} and T_M.

Finally, the results of the parameterized weld cross sections and temperature histories constructed according to Tables 1-21 contribute to a continually evolving database of weld cross sections and temperature histories corresponding to specified weld processes, process conditions and types of metals and their alloys. It follows that, given sufficient accumulation of parameterized weld cross sections and temperature histories spaning a wide range of process conditions, further investigation should concern determination of an optimal structure for this database.

Conclusion

The objective of this report is to describe a quantitative inverse thermal analysis of Ti-6Al-4V pulsed-mode laser welds corresponding to various weld process parameters and to construct numerical-analytical basis functions that can be used by weld analyst to calculated weld temperature histories, which are for welding processes associated with similar process conditions. This report contributes to the continuing evolution of parametric representations of temperature fields for inverse thermal analysis of welds associated with different types of metals, their alloys and weld process conditions. The weld temperature histories obtained by inverse analysis could in practice be used to predict not only solid-state phase transitions, but time and temperature within localized spatial regions associated with the evolution of plastic and elastic strains, resulting in distortion and residual stresses. Finally, the inverse analysis presented here concerns construction of a parametric temperature field, where it is assumed that the quantities κ ,V, l and isothermal surfaces $T(\hat{x}) = T_M$ or T_{TB} are known or reasonbly estimated. As emphasized previously [1], solidification and transformation boundaries are not the only quantities that are experimentally observable, and thus not the only quantities adoptable as constraint conditions for purposes of inverse thermal analysis.

Acknowledgement

This work was supported by a Naval Research Laboratory (NRL) internal core program.

References

1. S.G. Lambrakos, A. Shabaev and L. Huang, “Inverse Thermal Analysis of a Titanium Laser Weld Using Multiple Constraint Conditions,” Journal of Materials Engineering and Performance, published online 2014, DOI: 10.1007/s11665-014-1021-9.
2. S.G**.** Lambrakos and S.G. Michopoulos, Algorithms for Inverse Analysis of Heat Deposition Processes, ‘Mathematical Modelling of Weld Phenomena,’ Volume 8, 847, Published by Verlag der Technischen Universite Graz, Austria (2007).
3. S.G. Lambrakos and J.O. Milewski, Analysis of Welding and Heat Deposition Processes using an Inverse-Problem Approach, Mathematical Modelling of Weld Phenomena, **7**, 1025, Publishied by Verlag der Technischen Universite Graz, Austria 2005, pp. 1025-1055.
4. A. Tarantola, “Inverse Problem Theory and Methods for Model Parameter Estimation,” SIAM, Philadelphia, PA, 2005.
5. M.N. Ozisik and H.R.B. Orlande: Inverse Heat Transfer, Fundamentals and Applications, Taylor and Francis, New York, 2000.
6. K. Kurpisz and A.J. Nowak: Inverse Thermal Problems, Computational Mechanics Publications, Boston, USA, 1995.
7. O.M. Alifanov, Inverse Heat Transfer Problems, Springer, Berlin, 1994.
8. H. S. Carslaw and J. C. Jaegar: Conduction of Heat in Solids, Clarendon Press, Oxford, 2nd ed, 374, 1959.
9. E. Akman, A. Demir, T. Canel and T. Sinmazcelik, Laser Welding of Ti6Al4V Titanium, J. Mater. Proc. Tech, 209 (2009) pp. 3705-3713.